Front. Earth Sci. 2025, 19(4): 505–520
https://doi.org/10.1007/s11707-025-1169-7

RESEARCH ARTICLE

Genetic mechanism of deep zeolite-rich reservoirs: a case study of the Lower Wuerhe Formation in Junggar Basin

Tianxin HU[1], Yongqiang QU[2], Jian WANG[3], Junjun ZHOU[1], Wenfeng GE[1], Chenyu FU[1], Haiguang WU (✉)[1]

1 State Key Laboratory of Continental Shale Oil, Northeast Petroleum University, Daqing 163318, China
2 Research Institute of Petroleum Exploration and Development Northwest Branch, Lanzhou 730020, China
3 Experimental Testing Research Institute of PetroChina Xinjiang Oilfield Company, Karamay 834000, China

Abstract With continued exploration and the increased need for energy resources, deep reservoirs have gradually become the main target of oil and gas exploration in recent years. The Lower Wuerhe Formation on the northern slope of the Central Depression of the Junggar Basin has a high-quality, deep, glutenite (coarse-grained clastic) reservoir at depths greater than 4500 m. However, its genetic mechanism remains unclear. Here, we improve our understanding of the origin of this deep reservoir by performing comprehensive investigations via thin section analysis, field emission scanning electron microscopy, electron probe analysis, X-ray diffraction analysis, and whole-rock carbon and oxygen isotope analysis. The results reveal that the deep reservoir lithology within the study area comprises primarily gray-white gravelly gritstone and conglomerate. Zeolite cement is predominant, and secondary dissolution pores are the primary type of reservoir space in deep reservoirs. The Lower Wuerhe Formation has experienced significant compaction in the study area. Debris flow microfacies serve as the prevailing sedimentary microfacies containing substantial amounts of laumontite. The effect of dissolution of organic acids on laumontite is pivotal in the formation of high-quality deep reservoirs in the study area. These findings serve as valuable references for the genesis of deep zeolite-rich reservoirs in the Central Depression of the Junggar Basin and other areas worldwide.

Keywords deep reservoirs, laumontite, organic acid fluids, Lower Wuerhe Formation, Junggar Basin, genesis

1 Introduction

Oil and gas reservoirs in deep layers have gradually become important targets for exploration worldwide. Many deep oil and gas reservoirs have been discovered. For example, the burial depth of the target layer of the Kaskida oil and gas field in the Gulf of Mexico is 7356 m (Jia et al., 2011), that of the Washington oil field is 6540 m (Zhang et al., 2014), that of the Mills Ranch Field in the Anadarko sag ranges from 7663 m to 8103 m (Aase and Walderhaug, 2005), and that of the deep gas field under the Kelasu salt in the Tarim Basin is 7000 m (Pang, 2010). However, the genetic mechanism of deep reservoirs is very complex and varies from formation to formation. For example, the glutenite (coarse-grained clastic) reservoirs of the Kongdian Formation in the south-west Bozhong sag represent a typical sieve-like pore deposit. Its characteristics are influenced primarily by subsequent dissolution processes (Hou et al., 2019). However, the main factors controlling the physical properties of deep reservoirs in the Wufeng–Longmaxi Formations within the Sichuan Basin are predominantly related to sedimentary facies, such as the formation pressure coefficient and the presence of a deep-water microfacies sedimentary environment enriched with organic acids (Gao et al., 2022). The physical properties of deep reservoirs in the northern margin of the Qaidam Basin are controlled mainly by sedimentation, diagenesis, and abnormally high-elevation zones (Tian et al., 2022). Therefore, because of the uncertainty of deep reservoir genesis, it is necessary to further study the main factors controlling deep reservoirs on a case-by-case basis.

The Permian strata within the Junggar Basin are widely distributed and are important for exploration endeavors. As exploration in the Junggar Basin continues to advance, a burgeoning focus has been on probing deep reservoirs (He et al., 2021a). In the Junggar Basin, reservoirs buried more than 4500 m are usually regarded as deep layers by predecessors and have been continuously investigated in previous studies (Yao et al., 2018; Li et al., 2020b; Long

Received July 18, 2023; accepted April 17, 2025

E-mail: wuhg@nepu.edu.cn

et al., 2021; Huang et al., 2024; Liu et al., 2025). In recent years, notable oil and gas reservoirs have been discovered across a vast expanse within the middle and shallow layers of the Permian Wuerhe Formation, encompassing an expansive exploration area of approximately 1060 km^2. Moreover, the Lower Wuerhe Formation presents a resource potential capable of fostering substantial oil and gas fields (He et al., 2021b), indicating promising exploration prospects (Tang et al., 2023).

Previous studies have shown that fan delta sedimentary systems have developed in the Lower Wuerhe Formation in the Junggar Basin and that the lithology is dominated by glutenite (Pang, 2015), which is mainly rich in zeolite (Wang et al., 2018). The deep reservoirs in the basin exhibit obvious low-porosity and low-permeability characteristics (Qian et al., 2021a; Liu et al., 2024). The deep reservoirs of the Lower Wuerhe Formation have undergone various diagenetic processes, including compaction (Fu et al., 2019; Zou et al., 2021), cementation (Wang et al., 2018), and dissolution (Jiang et al., 2012; Wang et al., 2022a). Some scholars have suggested that low geothermal gradients and increased contents of rigid particles increase the number of primary pores in deep reservoirs, and these factors are the main factors controlling the formation process of high-quality deep reservoirs in the Lower Wuerhe Formation (Lei et al., 2020; Wang et al., 2022b). Moreover, some scholars have suggested that the shrinkage of zeolite during diagenesis increases secondary pores in deep reservoirs, where this factor is the main factor controlling the formation of high-quality deep reservoirs in the Lower Wuerhe Formation (Aase and Walderhaug, 2005). Most scholars have suggested that the dissolution of fluids in deep reservoirs is the greatest influence (Xu et al., 2018; Zhang et al., 2022; Han et al., 2023). However, sufficient evidence that dissolution is the main factor controlling high-quality deep reservoirs in the relevant formations is lacking. Moreover, the principal components of the acidic fluids involved in dissolution in the deep reservoirs of this formation have not been determined. In addition, although the presence of zeolites in the deep zeolite-rich reservoirs of the research area leads to complexity of soluble components in deep reservoirs (Meng et al., 2020), the genetic mechanisms of the deep reservoirs in the research area are diverse (Chen et al., 2014; Yuan et al., 2015), and the main dissolved components in the deep reservoirs have not yet been revealed. In summary, research on diagenesis and the genetic mechanism of high-quality deep reservoirs is urgently needed.

In this study, microscopic identification, C-O isotope analysis, field emission scanning electron microscopy (FE-SEM), electron probe microanalysis (EPMA), and X-ray diffraction (XRD), along with other rock–mineral analysis methods, were used to clarify the characteristics of physical properties and genesis of the deep glutenite reservoir in the Lower Wuerhe Formation on the northern slope of the central depression area. The mechanisms underlying the effects of the sedimentary environment and diagenesis on the physical properties of reservoirs are coupled, and their patterns of distribution are analyzed. This work provides a reference for the characteristics and genesis of deep zeolite-rich reservoirs worldwide.

2 Geological setting

The Junggar Basin is in north-western China and partially in the Xinjiang Uygur Autonomous Region. It is China's second-largest sedimentary basin (Li et al., 2020a; Qian et al., 2021b). The north-eastern region is adjacent to the Chingrid Mountains and the Kelamei Mountains, the western region is adjacent to the Zaire Mountains and the Hala'alat Mountains, and the southern region is adjacent to the north Tianshan Mountains and the Bogda Mountains (Fig. 1). The basin is approximately 700 km in length from east to west, 370 km in width from north to south, and encompasses an area of 136000 km^2.

The central depression zone is located in the middle of the basin, including five uplifts and five sags, for a total of ten secondary tectonic units, covering the main hydrocarbon-generating sags of the basin (Yin et al., 2008). Since the late Hercynian, the basin has experienced four tectonic stages—Hercynian, Indosinian, Yanshan, and Himalayan—and three basin stages—foreland, depression, and foreland. Under the transformation of multistage tectonic movements, a series of unconformity surfaces and faults have formed in the central depression area, and these surfaces and faults can provide a system for transporting oil and gas, and its peripheral structures have extraordinary oil and gas exploration potential (Ma et al., 2021).

The study area is located within the northern slope region of the central depression, which is located on the north-west margin of the Junggar Basin (Fig. 1). The northern slope area, which trends in a north-east–south-west direction, is adjacent to the Wuxia thrust fracture zone and Kebai fracture zone on the north-west margin. The structural and sedimentary evolution of this area has been influenced primarily by the thrust fracture zone on the north-west margin (Yuan et al., 2017; Qian et al., 2021a).

The stratigraphy in the study area exhibits a relatively complete sequence, with formations arranged from bottom to top as follows: the Permian Fengcheng Formation (P_1f), Xiazijie Formation (P_2x), and Lower Wuerhe Formation (P_2w); the Triassic Baikouquan Formation (T_1b), Karamay Formation (T_2k), and Baijiantan Formation (T_3b); the Jurassic Badaowan Formation (J_1b), Sangonghe Formation (J_1s), Xishanyao Formation (J_2x), and Toutunhe Formation (J_2t); the

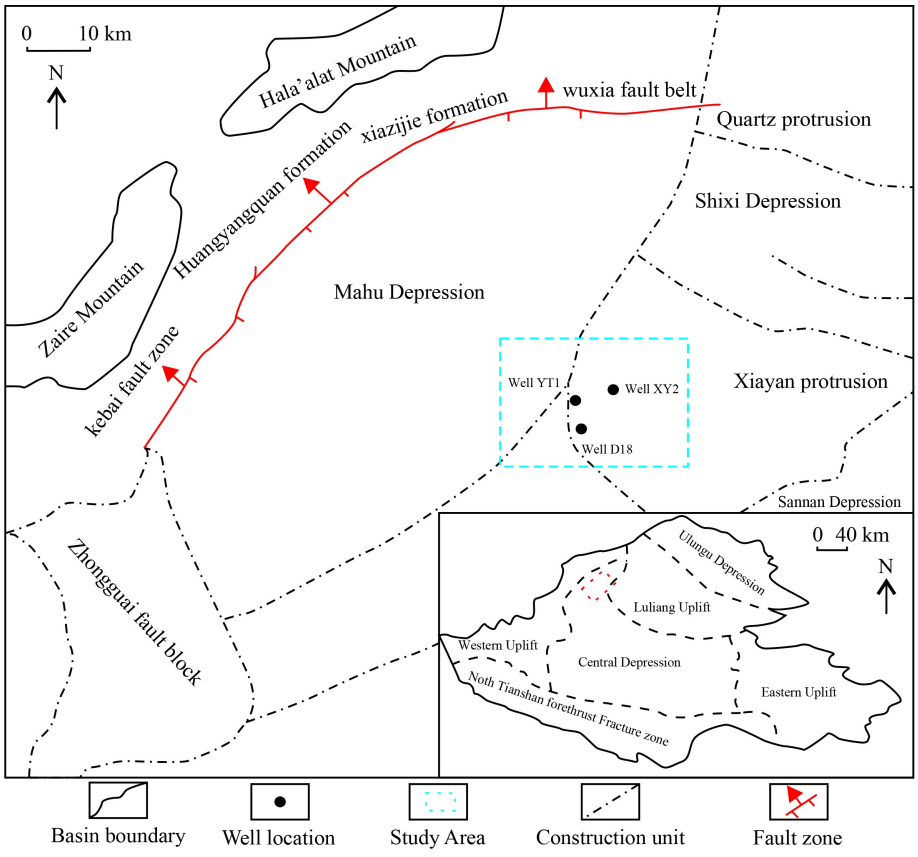

Fig. 1 Geographical location map of the study area.

Cretaceous Tugulu Group (K_1tg), Ailik Lake Formation (K_2a), and Hongyishan Formation (K_2h); the Palaeogene Ziniquanzi Formation ($E_{1-2}z$) and Anjihaihe Formation ($E_{2-3}a$); the Neogene Shawan Formation (N_1s), Tasihe Formation (E_3N_1s), and Dushanzi Formation (N_2d); and the Quaternary Xiyu Formation (Q_1x). All of these formations have regional unconformities between the Carboniferous and Permian, Permian and Triassic, Triassic and Jurassic, Jurassic, and Cretaceous, and Palaeogene and Neogene strata (Xia et al., 2012). The Lower Wuerhe Formation in the research area is in conformable contact with the underlying Xiazijie Formation (Chen et al., 2003) and is in unconformable contact with the overlying Baikouquan Formation (Wu et al., 2022). The Lower Wuerhe Formation can be subdivided into four sections: the first section (P_2w_1), the second section (P_2w_2), the third section (P_2w_3), and the fourth section (P_2w_4).

The Junggar Basin strata were deposited in a continental sedimentary environment with relatively active diastrophism, resulting in the formation of a faulted basin (Li et al., 2018; Tang et al., 2018). Various sedimentary systems within the faulted basin, including rivers, lakes, and alluvial fans, have influenced sediment deposition (Wang et al., 2020; Yu et al., 2023). The sedimentary facies of the Lower Wuerhe Formation have been classified into fan delta facies and lake facies. The sedimentary microfacies within the research area can be further classified into various types, including debris flow, braided channel, underwater distributary channel, estuarine sandbar, sheet sand, front fan delta, and semideep lake sedimentary microfacies (Hu et al., 2021; Wang et al., 2023). The evolution of these sedimentary facies exhibits a certain degree of continuity (He et al., 2018).

3 Methods

A total of 73 samples were collected from three wells, namely, D18, XY2, and YT1, containing the Permian Lower Wuerhe Formation. Thirty-seven samples were collected from Well D18, 16 samples were collected from Well XY2, and 20 samples were collected from Well YT1. The collection depths ranged from 4200 m to 5400 m, corresponding to deep to ultradeep layers, with layer thicknesses varying from 180 m to 1200 m.

All samples were finely ground into thin sections and subjected to microscopic examinations for rock and mineral identification to determine their mineral composition and structural characteristics. Additionally, 31 representative samples were subjected to microscopic pore observations via field emission scanning electron microscopy (FE-SEM) and electron probe microanalysis.

Scanning electron microscopy was conducted at Hunan Nanomicro New Materials Technology Co., Ltd., in the laboratory, employing a Sirion 200 field emission scanning electron microscopy instrument, which operated at a voltage of 10 kV and offered a resolution of 1.5 nm.

Electron probe microanalysis was conducted at the Testing Center of the Shandong Bureau of the China Metallurgical Geology General Administration. The testing instrument that was used was the JXA-8230 (JEOL) electron probe analyzer, with a working voltage of 15 kV, a working current of 20 mA, and a beam spot of 2 μm.

The research area consists primarily of conglomerate formations. During the preparation of rock sample powders, all gravel components were systematically removed, allowing for the exclusive grinding of the matrix material into powder. The mineral mass fractions of 18 representative samples were determined through X-ray diffraction. Analyses were conducted at the Hunan Nano New Material Science and Technology Co., Ltd., laboratory, utilizing a D/MAX 2500 Diffractometer. The test conditions for the whole rock sample powder were as follows: a copper target, voltage of 40 kV, current of 80 mA, step width of 0.02°, and scanning range of 3° to 60°. Data processing and analysis were subsequently performed via Jade 6.0 software, which involved identifying and calculating the heights of various mineral diffraction peaks on the basis of the X-ray diffraction analysis method for clay minerals and common nonclay minerals in sedimentary rocks. This process enabled the identification of different mineral types.

Stable carbon–oxygen (C–O) isotope analyses were conducted at the State Key Laboratory of Endogenetic Metal Deposits Metallogenic Mechanism Research, Nanjing University, using a continuous flow mass spectrometer (MAT 253). The $\delta^{13}C$ and $\delta^{18}O$ values were measured by analyzing the CO_2 released from the samples and comparing them with the LAEAC01 standard. The samples were dissolved in an H_3PO_4 solution at 70°C for a minimum of 2 h. The error for the $\delta^{13}C$ value was ± 0.03‰, and the error for the $\delta^{18}O$ value was ± 0.08‰. The results are reported in units of per mil relative to the Pee Dee Belemnite (PDB).

4 Results

4.1 Lithofacies

The Wuerhe Formation on the northern slope of the central depression was formed in a fan delta sedimentary system (Zhang et al., 2015; Zhou et al., 2023). In Well XY2, the combined microfacies sequence from top to bottom represents the environments of an underwater distributary channel, sheet sands, an underwater distributary channel, an estuary sand dam, and a third underwater distributary channel (Fig. 2(a)). In Well YT1, the combined microfacies sequence from top to bottom consists of a pre-fan delta, an underwater distributary channel, sheet sands, a debris flow, a pre-fan delta, and a second debris flow (Fig. 2(b)). In Well D18, the combined microfacies sequence from top to bottom represents the environments of a semideep lake, a debris flow, sheet sands, an underwater distributary channel, and a second debris flow (Fig. 2(c)).

The debris flow sedimentary microfacies consists primarily of gray-black conglomerate and fine conglomerate. The thicknesses of a single layer range from 0.65 m to 1.5 m. Overall, the gravel clasts are relatively small in size, and the argillaceous content is low. The grains are poorly sorted and angular to subrounded.

The underwater distributary channel facies in the study area consist of gray thin argillaceous siltstone, siltstone, fine sandstone, coarse sandstone, gravel-bearing medium sandstone, and thin-layer conglomerate. The main lithology is medium- to coarse-grained sandstone, which originated from traction flow. The conglomerate has uniformly sized gravel and is particle supported, moderately sorted, and well rounded; in addition, it consists of mainly subcircular to subangular grains, and the conglomerate is massive in structure. Owing to the superposition of multistage channel sand bodies, the thickness can reach 4.87 m. This layer consists mostly of medium–fine sandstone, and the thickness of a single layer is not greater than 0.5 m.

The thicknesses of the sheet sand body are 0.2–2.2 m, and its lithologies are mainly gray siltstone, mixed fine sandstone, argillaceous siltstone, and mudstone. The particle sorting and rounding are poor, the grains are mainly subangular, and some of the siltstone features asphalt and block structures. Its bottom often abruptly contacts the coarse sandstone and gravel-bearing medium sandstone deposited in the underwater distributary channel microfacies.

The predelta subphase in the study area is mainly in Well YT1 and consists of gray-green, gray-black mudstone, argillaceous siltstone, and thin-layered gray-white siltstone. Horizontal bedding has developed, and the sedimentary thickness is approximately 3 m.

The semideep lake deposits in the study area are relatively developed. The lithology is gray–black mudstone, with thicknesses of 0.15–2.0 m, and horizontal bedding has developed, reflecting the sedimentary characteristics of weak wave action in a lake.

Core observations indicate the presence of a fan delta front facies sandy conglomerate within the Lower Urho Formation in the study area, with the predominant rock types of the reservoir being greyish white massive gravelly gritstone and conglomerate (Figs. 2(a) and 2(b)). The cement content between rock debris particles is notably high, primarily consisting of zeolite cement with

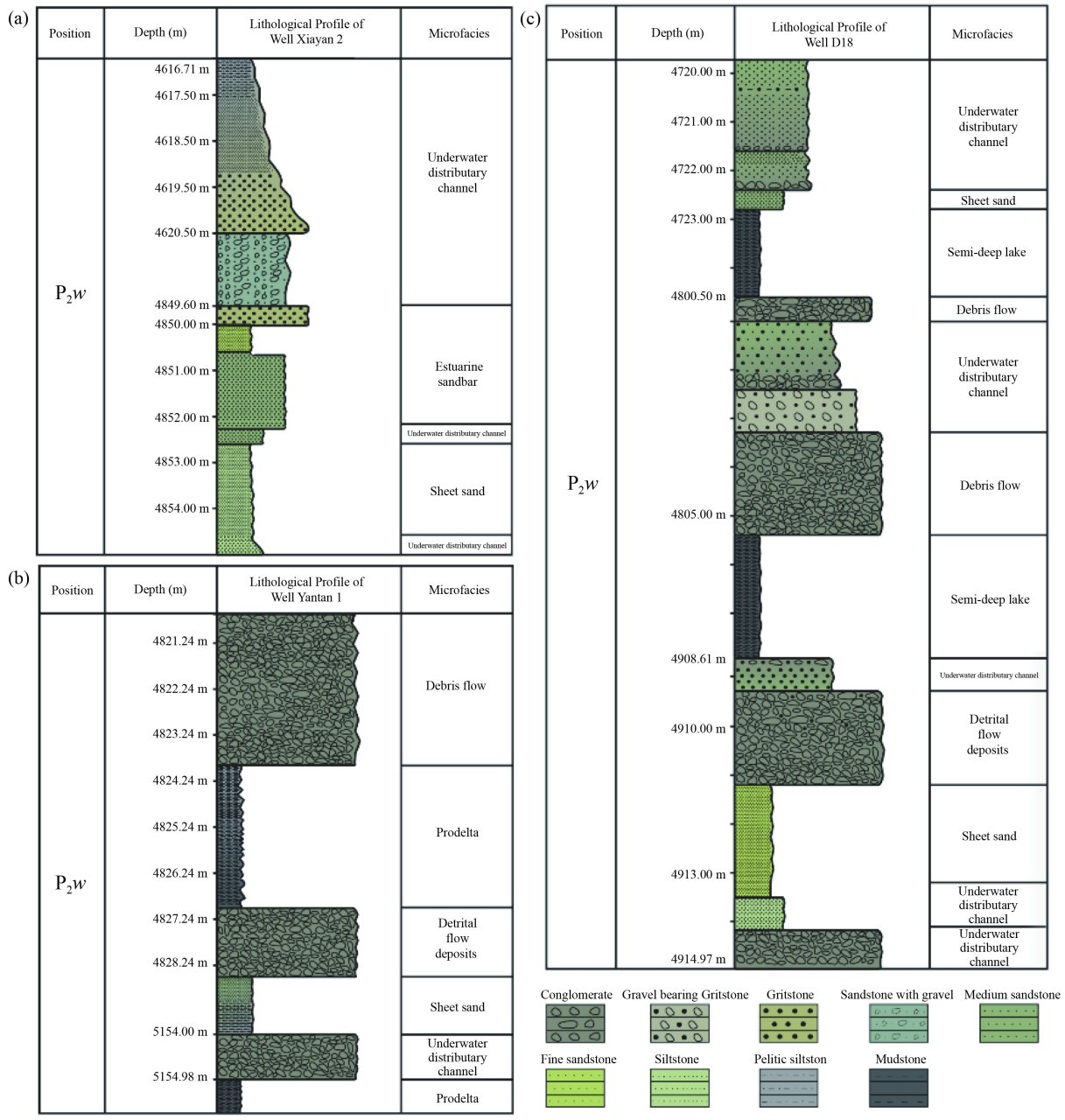

Fig. 2 Comprehensive stratigraphic column of sedimentary microfacies in the core section of the Lower Wuerhe Formation. (a) Well XY2; (b) Well YT1; (c) Well D18.

minor calcite (Figs. 3(c) and 3(d)). The cement type significantly impacts the reservoir; zeolite cement and carbonate cement are the main types observed. Zeolite cements are found mostly in the intergranular pores of sandy conglomerates, with coarser particles and less matrix (Figs. 3(e) and 3(f)).

Under microscopic examination, zeolite cement appears as plate-like or granular in structure, they are typically colorless or white and often exhibit complete cleavage. X-ray diffraction test data indicate that the overall mass fraction values of zeolite cement in the study area span from 1.48% to 23.34%, with an average content of approximately 9.74%.

There are multiple types of carbonate cements, including calcite, dolomite, and siderite, each with varying contents. The overall mass fraction values of carbonate cement range from 0.43% to 13.52%, with an average mass fraction of 3.61%. The average mass fraction content of the calcite cement is 2.06%, that of the dolomite cement is 0.97%, and that of the siderite cement is 0.58% (Table 1).

4.2 Geochemical characteristics

Electron probe analysis was conducted on zeolite samples obtained from Well D18 and Well XY2, which exhibit

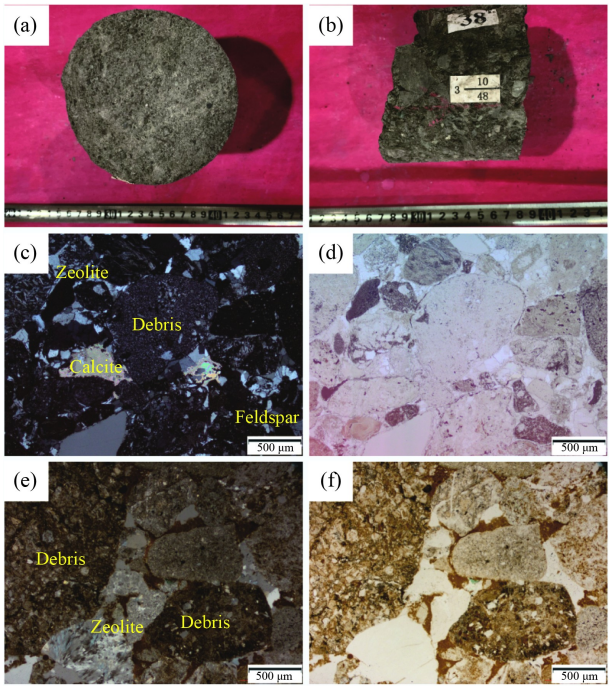

Fig. 3 Cores and micrographs of the Lower Wuerhe Formation sand and gravels in the study area. (a) Well D18, 4721.9 m, containing gravelly gritstone with mud particles locally; (b) Well YT1, 4972.86 m, gray black block conglomerate with obvious cement filling; (c) Gravel bearing gritstone (×5, orthogonal polarization); (d) Gravel bearing gritstone (×5, single polarized light); (e) Conglomerate (×5, orthogonally polarized); (f) Conglomerate (×5, single polarized light).

physical properties that are favorable in the study area. The analysis reveals average Na_2O contents of 0.207%, SiO_2 contents ranging from 49.651% to 55.727%, FeO and MnO contents of 0.052% and 0.006%, respectively, CaO contents ranging from 10.605% to 11.134%, and Al_2O_3 contents ranging from 20.59% to 21.89%, with an average content of 21.09%. The Si/Al ratios range from 2.398 to 2.691, and the average total content is 86.573% (Table 2). These components indicate that the zeolite in the study area is mainly laumontite, whereas the calcite is divided into early calcite and late calcite, which is consistent with the results of previous studies (Huang et al., 2015; Gao et al., 2017). FE-SEM analyses reveal that horizons with higher laumontite contents present a greater number of dissolution pores. These dissolution pores are well developed, manifesting as bay-shaped, serrated, and concave–convex-shaped structures, with evident signs of laumontite dissolution (Fig. 4).

4.3 Characteristics of the physical and reservoir space

4.3.1 Reservoir physical properties

The results of physical property testing of the core samples indicate that the porosities of the deep reservoirs within the Lower Wuerhe Formation in the study area range predominantly between 10% and 15% (Fig. 5(a)), with an average porosity of 10.67%. Ultralow-porosity reservoirs (porosity < 10%) account for 37.86% of the total reservoir volume, whereas low-porosity reservoirs (porosities ranging from 10% to 15%) comprise 53.21% (Fig. 5(b)). The reservoir permeabilities range primarily between 0 mD and 5 mD (Fig. 5(c)), with an average permeability of 12.17 mD. The medium-permeability reservoirs (50–500 mD) account for approximately 5.38%, the low-permeability reservoirs (5–50 mD) account for approximately 10.75%, and the tight reservoirs (< 5 mD) represent approximately 83.87% of the total. According to the Clastic Rock Reservoir's

Table 1 X-ray diffraction data of the Permian Lower Wuerhe Formation strata in the study area

Mineral type	Quartz	Feldspar	Zeolite	Calcite	Dolomite	Siderite	Clay mineral	Summation
D18-2	12.83%	59.17%	11.15%	1.33%	1.94%	0.86%	12.72%	100.00%
D18-10	15.34%	61.21%	5.40%	0.71%	1.10%	0.49%	15.74%	100.00%
D18-14	15.25%	44.21%	23.34%	2.69%	1.29%	0.89%	12.33%	100.00%
D18-17	22.50%	35.56%	16.80%	1.68%	1.80%	0.67%	20.99%	100.00%
D18-25	21.71%	46.49%	1.48%	0.43%	0	0	29.89%	100.00%
XY2-1	15.18%	53.04%	3.91%	12.18%	0.90%	0.44%	14.35%	100.00%
XY2-5	18.04%	64.99%	4.55%	0.78%	0	0.47%	11.18%	100.00%
XY2-15	22.32%	37.13%	22.58%	2.49%	1.76%	0.91%	12.81%	100.00%
XY2-18	19.44%	38.88%	8.56%	0.64%	1.03%	0.81%	30.63%	100.00%
XY2-21	16.96%	61.97%	1.69%	0.47%	0	0	18.91%	100.00%
XY2-22	17.67%	52.01%	12.60%	1.37%	0.97%	1.37%	14.02%	100.00%
YT1-3	11.08%	62.54%	4.78%	0	0.82%	0	20.78%	100.00%
YT1-4	12.73%	55.76%	10.62%	0.97%	0.73%	0.55%	18.64%	100.00%
YT1-7	16.63%	58.57%	7.53%	0.43%	0.25%	0.41%	16.18%	100.00%
YT1-12	14.58%	53.69%	11.16%	1.34%	0.32%	0	18.91%	100.00%

Table 2 Electron probe test data of Permian Lower Wuerhe Formation stratigraphy in the study area

Well	Depth	Point number	Elemental composition/(wt.%)								Total	Mineral
			Na_2O	SiO_2	FeO	MnO	CaO	Al_2O_3	TiO_2	Si/Al		
D18	4804.3	1	0.248	54.761	0	0	11.144	21.336	0.002	2.567	87.614	Laumontite
	4804.3	2	0.266	54.868	0	0.003	11.167	21.34	0.007	2.571	87.785	Laumontite
	4804.3	3	0.112	54.365	0.078	0	11.556	21.76	0.022	2.498	88.183	Laumontite
	4804.3	4	0.098	53.764	0.019	0	11.921	21.811	0	2.465	87.756	Laumontite
	4804.3	5	0.268	54.926	0.043	0	11.463	21.59	0.002	2.544	88.439	Laumontite
	4804.3	6	0.304	53.445	0.027	0.019	10.933	20.705	0	2.581	85.574	Laumontite
	4804.3	7	0.410	55.727	0.018	0.032	10.903	20.864	0.001	2.671	88.107	Laumontite
	4804.3	8	0.394	55.368	0.028	0	10.893	20.929	0.013	2.646	87.832	Laumontite
	4804.3	9	0.237	53.408	0.029	0	11.574	21.293	0.032	2.508	86.654	Laumontite
	4804.3	10	0.148	54.203	0.022	0	10.859	20.725	0.016	2.615	86.135	Laumontite
	4804.3	11	0.083	53.086	0.313	0	10.912	21.073	0.012	2.519	86.568	Laumontite
	4804.3	12	0.016	1.376	0.080	0.057	55.636	0.008	0.005	0.571	57.749	Early calcite
	4804.3	13	0.025	0.016	0.046	0.095	56.581	0.006	0	0	56.769	Early calcite
D18	4802.3	1	0.325	54.775	0.062	0	11.091	21.071	0	2.6	87.434	Laumontite
	4802.3	2	0.462	55.414	0	0	10.873	20.59	0	2.691	87.479	Laumontite
	4802.3	3	0.427	53.285	0	0	11.082	21.292	0.007	2.503	86.216	Laumontite
	4802.3	4	0.280	54.362	0.017	0	11.035	20.877	0.008	2.604	86.736	Laumontite
	4802.3	5	0.396	54.652	0.019	0	10.977	20.805	0.023	2.627	87.007	Laumontite
	4802.3	6	0.377	54.261	0.025	0.003	11.225	20.814	0.002	2.607	86.862	Laumontite
	4802.3	7	0.517	54.051	0.015	0	10.605	20.702	0.008	2.611	86.054	Laumontite
	4802.3	8	0.011	52.812	0.049	0	11.899	21.883	0.036	2.413	86.781	Laumontite
	4802.3	9	0.277	54.303	0.002	0.032	10.946	20.661	0	2.628	86.346	Laumontite
	4802.3	10	0.040	0.055	0.046	0.083	55.571	0	0.028	0.010	55.833	Late calcite
	4802.3	11	0.009	0.043	0.034	0.147	56.070	0.005	0.002	0	56.310	Late calcite
XY2	4616.9	1	0.071	53.364	0.06	0	11.007	20.767	0	2.57	85.392	Laumontite
	4616.9	2	0.067	49.651	0.214	0.035	11.482	20.704	0	2.398	83.132	Laumontite
	4616.9	3	0.062	53.955	0.055	0	11.261	20.849	0.004	2.588	86.295	Laumontite
	4616.9	1	0.071	53.364	0.06	0	11.007	20.767	0	2.57	85.392	Laumontite
	4616.9	2	0.067	49.651	0.214	0.035	11.482	20.704	0	2.398	83.132	Laumontite
	4616.9	1	0.240	53.657	0.051	0	11.240	21.297	0.015	2.519	86.621	Laumontite
	4616.9	2	0.158	54	0.069	0	11.383	21.226	0.026	2.544	86.971	Laumontite
	4616.9	3	0	53.568	0.057	0.019	11.386	21.389	0.044	2.504	86.536	Laumontite
	4616.9	1	0.020	53.084	0	0	11.666	21.406	0.008	2.48	86.252	Laumontite
	4616.9	2	0.002	51.544	0	0.003	11.831	21.264	0	2.424	84.738	Laumontite
	4616.9	3	0	53.338	0	0.016	12.134	21.885	0	2.437	87.383	Laumontite
	4616.9	1	0.361	54.633	0.018	0.008	11.285	20.703	0	2.639	87.177	Laumontite
	4616.9	2	0.056	53.583	0.067	0	11.530	20.811	0	2.575	86.339	Laumontite

Physical Property Classification Standard, the reservoirs within the Lower Wuerhe Formation are categorized as low-porosity and low-permeability reservoirs. In addition, the relationship between the porosity and depth of the deep reservoir of the Lower Wuerhe Formation reveals that at burial depths greater than 4500 m, there is still an abnormally high porosity zone (Fig. 5(d)) that deviates from the normal compaction curve.

4.3.2 Reservoir space characteristics

The reservoir contains a relatively high proportion of rock

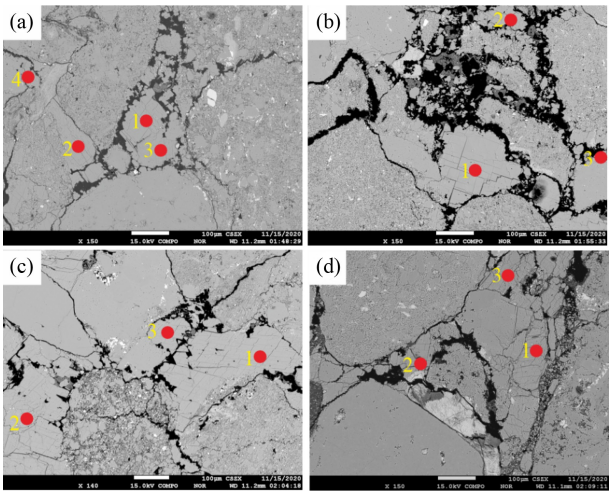

Fig. 4 Back scattered electron microscopic images. (a) Well D18, 4804.3 m, with laumontite dissolution in a harbor-like manner; (b) Well D18, 4802.3 m, with obvious signs of laumontite dissolution; (c) Well XY2, 4616.9 m, with large areas of laumontite cementation observed; (d) Well XY2, 4616.9 m, with a large amount of laumontite. (Please refer to for specific data).

debris, with the visible volume fraction under the microscope averaging 45% and reaching a maximum of 60%. The composition is primarily tuff. The rock grains are predominantly subangular and subrounded, exhibit poor to medium sorting and are supported by a matrix. Additionally, the reservoir contains a high shale content and appears massive to thickly layered. The quartz and feldspar clasts have a combined particle size of approximately 30%, and their contact relationship is characterized primarily by concave–convex and linear contacts. Notably, there is significant mineral compression and fragmentation.

The thin sections and SEM images indicate close particle-to-particle contacts within the reservoirs. The primary type of reservoir space that is identified is dissolution pores (Fig. 6), followed by residual intergranular pores. Dissolution pores are primarily intergranular and intragranular dissolution pores, with diameters typically ranging from 50 μm to 500 μm. Intergranular dissolution pores, reaching up to 500 μm, are formed predominantly through the secondary enlargement of primary intergranular pores and are commonly connected to fractures. The edges of these pores exhibit a harbour-shaped, serrated, and concave–convex structure (Fig. 6(a)), and they are

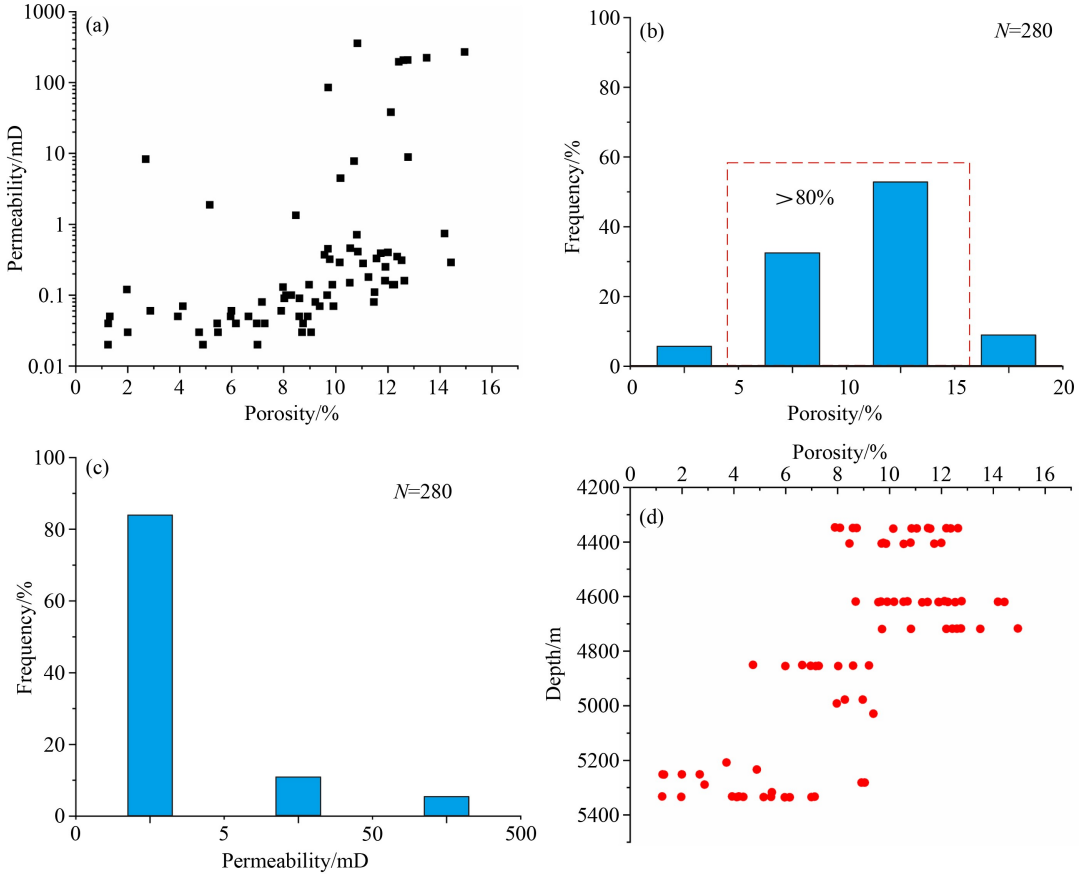

Fig. 5 Physical characteristics of the Lower Wuerhe Formation reservoirs in the study area. (a) Relationship between porosity and permeability of Lower Wuerhe Formation; (b) porosity distribution histogram of the Lower Wuerhe Formation glutenite reservoir; (c) permeability distribution histogram of the Lower Wuerhe Formation glutenite reservoir; (d) relationship between porosity and depth of the Lower Wuerhe Formation.

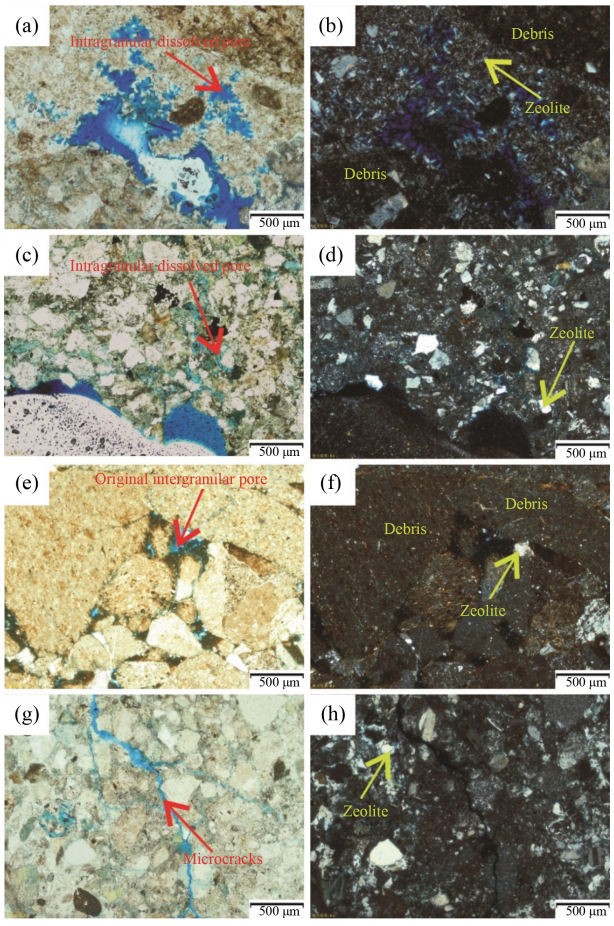

Fig. 6 Space type of conglomerate reservoir in the Lower Wuerhe Formation. (a) Well YT1, 5157.63 m, developed intergranular dissolution pores, intergranular zeolite cementation dissolution, with a maximum pore size of up to 500 μm, (×10, single polarized); (b) Well YT1, 5157.63 m (×10, orthogonal); (c) Well D18, 4917.94 m, feldspar dissolves along its cleavage surface, (×5, single polarized light); (d) Well D18, 4917.94 m (×5, orthogonal); (e) Well XY2, 4719.23 m, with a pore size of approximately 200 μm, connected to intergranular pores, (×5, single polarized); (f) Well XY2, 4719.23 m (×5, orthogonal); (g) Well D18, 4807.44 m, microcracks (×5, single polarized light) at the edge of gravel rock debris particles; (h) Well D18, 4807.44 m (×5, orthogonal).

distributed primarily near eroded rock debris and zeolite cement between rock debris particles (Fig. 6(b)). Intragranular dissolution pores result mainly from the selective dissolution of detrital particles (particularly feldspar) along cleavage planes or soluble components, with pore diameters typically ranging from approximately 50 μm to 100 μm. These pores are frequently linked with dissolution pores created by zeolite cement, displaying irregular harbour-like shapes with uneven edges (Fig. 6(c)). Some residual intergranular pores are observed, primarily representing spaces that remain after the primary intergranular pores undergo diagenetic evolution stages (Fig. 6(d)). These pores generally have diameters ranging from 50 μm to 200 μm and manifest as triangles, quadrilaterals, and irregular polygons (Figs. 6(e) and 6(f)). Microcracks can also be observed in several samples, resulting mainly from crack corrosion and expansion. Widths typically range from 10 μm to 20 μm. These cracks have a certain directionality, the ability to be filled, and corrosion expansion ability (Figs. 6(g) and 6(h)).

4.4 Characteristics of stable carbon and oxygen isotopes

To further investigate the mechanism of formation of dissolution pores, comprehensive whole-rock stable carbon and oxygen isotope analysis was conducted on representative samples from Wells D18, XY2, and YT1. The analysis reveals intriguing insights. The $\delta^{13}C$ values range from −0.08‰ to −18.72‰ (V-PDB), whereas the $\delta^{18}O$ values range from −19.19‰ to −13.25‰ (V-PDB) (Table 3). In particular, Well D18 exhibits $\delta^{13}C$ values ranging from −15.34‰ to −17.60‰, Well XY2 displays $\delta^{13}C$ values ranging from −11.30 ‰ to −14.29 ‰, and Well YT1 has $\delta^{13}C$ values ranging from −1.80 ‰ to −8.69 ‰. These findings align with previous research findings (Fu et al., 2019; Zhang, 2021; Sun et al., 2023).

5 Discussion

5.1 The influence of sedimentation on pores

It is crucial to study the composition types of dissolution

Table 3 C-O isotope data sheet of the Lower Wuerhe Formation in the study area

Well	Sample No	$\delta^{18}O$/(‰ V-PDB)	$\delta^{13}C$/(‰ V-PDB)
D18	D18-15	−17.53	−17.60
D18	D18-15	−17.26	−17.65
D18	D18-17	−15.96	−16.24
D18	D18-18	−19.19	−18.72
D18	D18-19	−15.88	−16.70
D18	D18-24	−16.80	−14.29
D18	D18-25	−14.39	−11.79
D18	D18-3	−15.86	−17.66
D18	D18-7	−17.02	−15.34
XY2	XY2-1	−18.91	−14.29
XY2	XY2-11	−19.40	−13.87
XY2	XY2-21	−14.95	−10.75
XY2	XY2-21	−14.71	−10.78
XY2	XY2-5	−16.44	−11.23
XY2	XY2-5	−16.62	−11.30
YT1	YT1-19	−18.03	−8.69
YT1	YT1-5	−14.67	−3.19
YT1	YT1-7	−16.73	−1.80
YT1	YT1-8	−13.25	−0.08

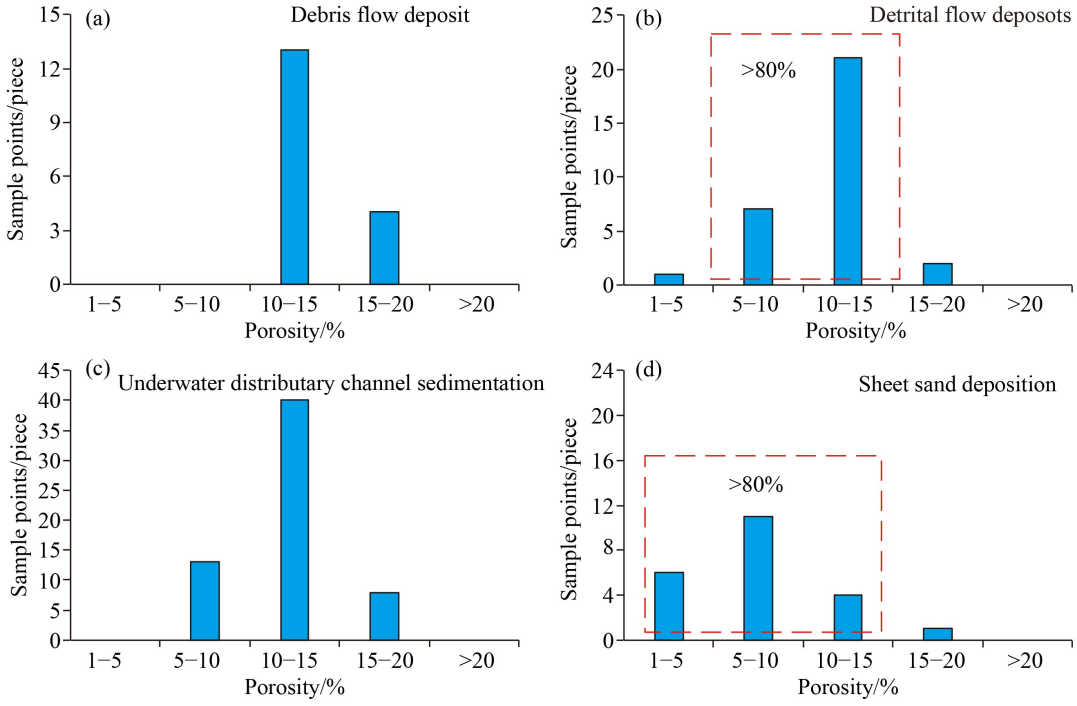

Fig. 7 Porosity distribution histogram of different sedimentary microfacies in P_2w of the North Slope. (a) Histogram of sediment porosity of debris flow sedimentation; (b) histogram of porosity in detrital flow deposits; (c) histogram of sedimentary porosity in underwater distributary channels; (d) histogram of porosity in the sheet sand deposits.

minerals under dominant sedimentary microfacies. Different sedimentary microfacies show significant differences. Statistical analysis was conducted on the porosity and permeability data obtained from three underground cored wells in the Wuerhe Formation: Well D18, Well XY2, and Well YT1. The analysis reveals the development of abnormally high-porosity zones within various sedimentary microfacies. The porosities of the conglomerates deposited by debris flows are primarily within 10% to 15%, with overall values ranging from 11.3% to 18.6% (Fig. 7(a)). The corresponding permeability values range from 0.01 mD to 458 mD (Fig. 8(a)). Similarly, for detrital flow deposits, the porosities range from 10% to 15%, with values ranging from 4.2% to 15.1% (Fig. 7(b)), and the permeability values range from 0.01 mD to 1428.2 mD (Fig. 8(b)), indicating the presence of samples with high permeability (> 500 mD). The underwater distributary channel deposits consist of conglomerate, gritstone, medium sandstone, and fine sandstone. The porosities in these deposits range primarily between 10% and 15%, with overall values ranging from 6% to 17% (Fig. 7(c)), and the corresponding permeabilities range from 0.01 mD to 80 mD (Fig. 8(c)). The porosities of the fine sheet sand siltstones range between 5% and 10%, with values ranging from 2.1% to 15.4% (Fig. 7(d)). The maximum permeability observed in this microfacies is 52.6 mD (Fig. 8(d)). These findings indicate that the physical properties of debris flow microfacies are the most favorable, followed by underwater distributary channel microfacies, whereas sheet sand microfacies exhibit relatively inferior physical properties.

5.2 Study of the dissolved components and sources of dissolution fluid

The formation of secondary pores through dissolution is the primary factor contributing to enhanced physical properties in deep reservoirs (Guo et al., 2017), underscoring the importance of studying their dissolution components. Therefore, the relationships among rock components, including zeolite, feldspar, and quartz contents, and the physical properties of the reservoir were analyzed. Overall, there is a positive correlation between the zeolite content and porosity/permeability (Figs. 9(a) and 9(b)). However, the correlations between the feldspar content and reservoir porosity and permeability are weak but positive (Figs. 9(c) and 9(d)). There is no significant correlation between the quartz content and reservoir porosity or permeability (Figs. 9(e) and 9(f)). These results suggest that zeolite is the primary dissolved component in reservoirs.

Moreover, the zeolite content and secondary pores are correlated (Figs. 9(a) and 9(b)). The significant presence of laumontite in the study area contributes to improved reservoir physical properties. The laumontite cement content in reservoirs is one of the principal factors controlling the physical properties of deep reservoirs.

An analysis of scatter plots depicting the whole-rock stable carbon and oxygen isotopes (Fig. 10(a)) provides

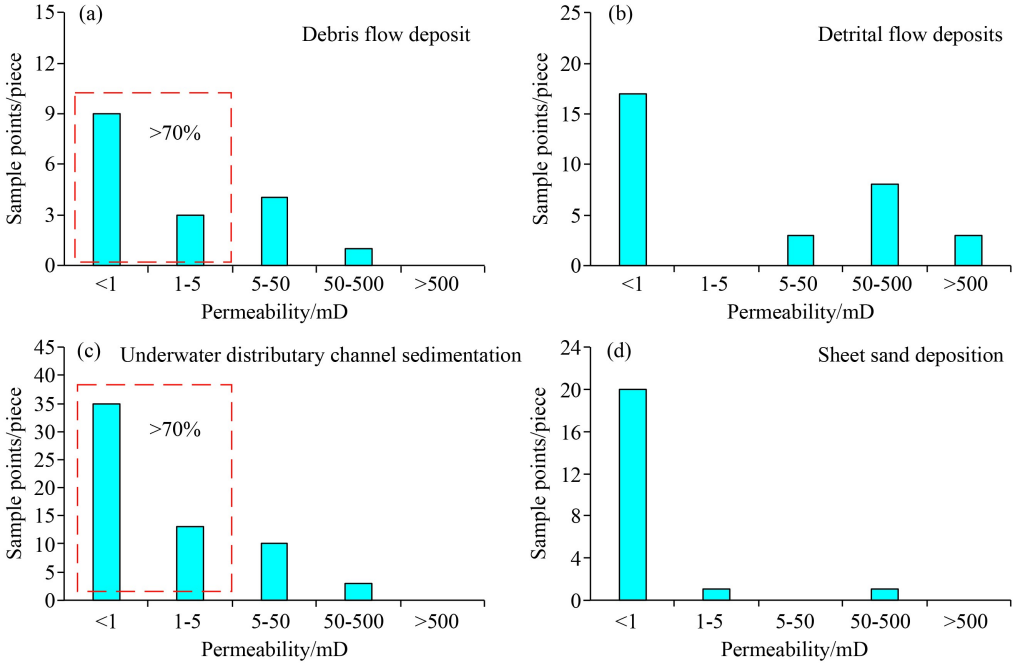

Fig. 8 Histogram of permeability distribution of different sedimentary microfacies in P_2w of the North Slope. (a) Histogram of sediment permeability of debris flow sedimentation; (b) histogram of sediment permeability of detrital flow deposits; (c) histogram of sediment permeability in underwater distributary channels; (d) histogram of permeability of sheet sand deposition.

valuable insights. The reservoir in Well D18 has the lowest $\delta^{13}C$ values, whereas that in Well YT1 has the highest $\delta^{13}C$ values. Well XY2, on the other hand, has values between those of the other two wells, i.e., intermediate $\delta^{13}C$ values. This is due to the inability of atmospheric fresh water to affect carbon isotope values. Previous studies have classified the sources of carbon isotopes into salt carbonate genesis, organic acid decarboxylation, and biogenic gas genesis. The stable carbon isotope values of organic acids are usually −25‰, while the decarboxylation of organic acids can result in stable carbon isotope values less than 0‰ (Wang et al., 2021). The abnormal $\delta^{13}C$ values indicate that the reservoir experienced dissolution by organic acid fluids during the later stages, resulting in the formation of numerous dissolution pores. Therefore, these findings suggest that Well D18 experiences prolonged interactions with organic acids, leading to a greater dissolution intensity. Well XY2 has a relatively moderate interaction intensity, whereas Well YT1 has the lowest intensity.

Finally, an analysis of the physical properties of these three representative drilling wells reveals fascinating results (Fig. 10(b)). The overall reservoir physical properties of Well D18 are the most favorable, followed by those of Well XY2, whereas Well YT1 has the least favorable physical properties. This result indicates that stronger contact between the reservoir and organic acid fluids is more likely to result in the development of high-quality reservoirs. Given the burial depth of approximately 4000 m in the research area, disregarding the impact of atmospheric precipitation on deep reservoirs is reasonable. Therefore, organic acid fluids have emerged as one of the key factors controlling the formation of high-quality deep reservoirs in the Lower Wuerhe Formation. In addition, the content of authigenic carbonate cement is not correlated with porosity or permeability, which implies that a significant quantity of calcite cement did not form during diagenesis (Fig. 10(c) and 10(d)).

5.3 Reservoir-forming mechanism

The Junggar Basin has a complex tectonic history and underwent many orogenic events, which undoubtedly affected the fractures and porosity and permeability characteristics of the reservoir rocks. However, through thin section identification and scanning electron microscopy analysis, the development of microcracks is not significant (Fig. 6). Overall, the debris flow microfacies are the dominant sedimentary microfacies. Frequent volcanic activity led to the devitrification of volcanic glass in volcanic rock debris-bearing glutenite and the formation of early unstable clinoptilolite (Weibel et al., 2019). Compaction caused by volcanic glass zeolitization, the formation of montmorillonite and cementation, such as calcareous cementation and zeolite cementation, are the main factors influencing the decrease in reservoir porosity. This also led to a rapid decrease in the porosity of the entire glutenite. As the burial of P_2w continued, the early clinoptilolite gradually underwent analcite formation and zeolitization, eventually transforming into laumontite and increasing the

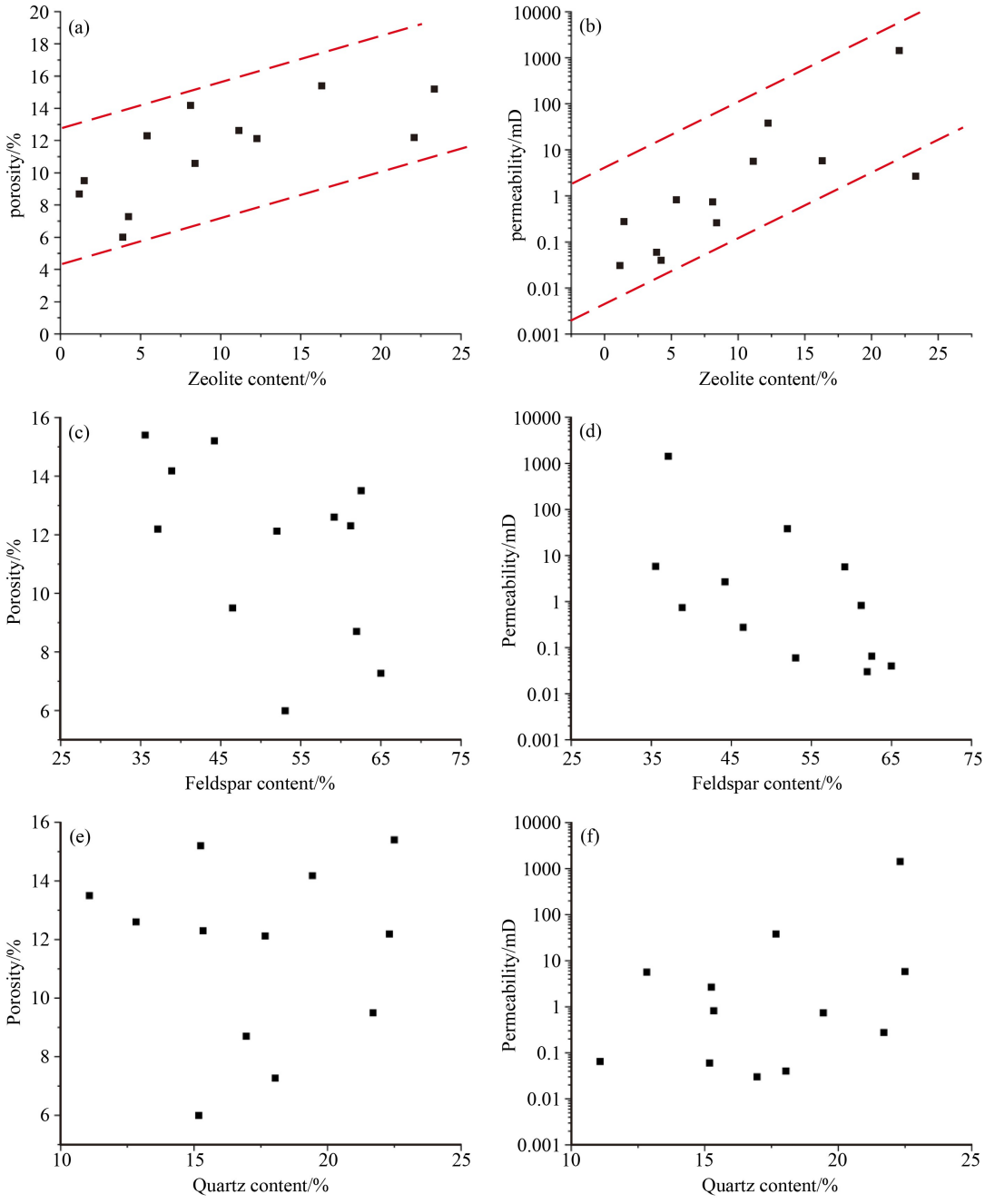

Fig. 9 Characteristics of zeolites and physical properties of the Lower Wuerhe Formation reservoirs in the study area. (a) Relationship diagram between porosity and zeolite content; (b) relationship between permeability and zeolite content; (c) relationship diagram between porosity and feldspar content; (d) relationship between permeability and feldspar content; (e) relationship diagram between porosity and quartz content; (f) relationship between permeability and quartz content.

proportion of laumontite. With the continuous increase in organic acids produced by the development of source rocks, laumontite continued to undergo dissolution, and the decrease in deep reservoir pores was alleviated (Fig. 11), indicating that organic acids and zeolite cements do not play a destructive role in reservoir pores, such as those in medium–shallow reservoirs but play a key role in increasing the number of pores in deep reservoirs.

Deep reservoirs are routinely exposed to intense compaction throughout the burial phase. The overburden pressure prompts a rearrangement of rock grains, typically culminating in the near-total obliteration of primary pores, given that the pores are highly susceptible to collapse under such compressive forces. However, in deep reservoirs rich in zeolite, the widely dispersed cementitious substances in zeolite have provided significant support. They initiated a robust cementation process that occurred early in the sedimentary history. This cementation has bolstered the sediment's ability to

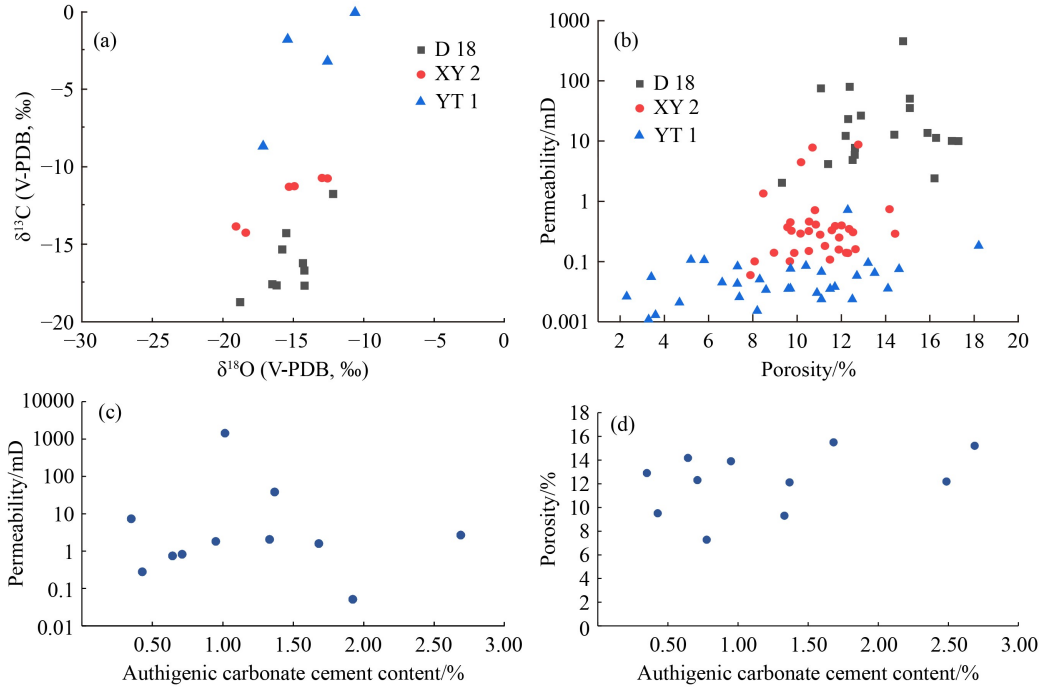

Fig. 10 Whole-rock stable carbon and oxygen isotope and physical scatter plot of the P_2w reservoir in the study area. (a) Scatter plot of stable carbon and oxygen isotopes throughout the rock; (b) scatter plots of physical properties at different well locations; (c) the diagram of the relationship between authigenic calcite and porosity; (d) the diagram of the relationship between authigenic calcite and permeability.

withstand compaction and, as a result, favored the preservation of primary pores. Zeolite acted as a protective framework that maintained the integrity of the pore structure. Concurrently, the presence of organic acids, which are commonly generated during the maturation of organic matter in source rocks, triggered significant dissolution within the reservoir. This dissolution represents a key controlling factor, as it causes an increase in a substantial number of secondary pores through chemical reactions with rock minerals. These secondary pores not only increase the overall porosity but also improve the pore connectivity. Consequently, the permeability of deep reservoirs has increased to a certain extent, thereby providing pathways for the migration of hydrocarbons. Collectively, the combined implications of these processes ultimately shape the characteristics and formation of deep reservoirs and govern their quality.

6 Conclusions

The deep reservoir lithology of the Permian Lower Wuerhe Formation in the central depression of the Junggar Basin is characterized primarily by greyish white massive gravelly gritstone and conglomerate. Within this region, deep, high-quality reservoirs are present, with zeolite cementation being the predominant cementation type and being abundantly distributed. The primary reservoir space is dominated by secondary dissolution pores. The debris flow microfacies exhibit the best physical properties among the deep reservoirs in the study area, followed by the underwater distributary channel microfacies, whereas the sheet sand microfacies present the least favorable physical properties.

Diagenesis in the study area is characterized primarily by compaction, cementation, and dissolution. Strong compaction adversely affects the development of primary pores and significantly hinders the physical properties of reservoirs. Conversely, the dissolution process yields dissolution pores that greatly enhance the physical properties of the reservoir. Zeolite cement, which is composed primarily of laumontite, plays a significant role in deep reservoirs. The laumontite content is positively correlated with reservoir physical properties, exerting a substantial influence on the physical properties of deep reservoirs in the study area. The fluids involved in dissolution responsible for the deep reservoirs in the study area are organic acids. The greater the dissolution strength of the deep reservoir is, the better the physical properties of the reservoir. Sedimentation and diagenesis are the main factors controlling the physical properties of deep reservoirs in the study area.

Conflict of Interest The authors declare no competing interests.

Acknowledgments The work was financially supported by the National Natural Science Foundation of China (Grant No.42372150) and Provincial University Basic Scientific Research Operating Cost Projects (No. 2023RCZX-02).

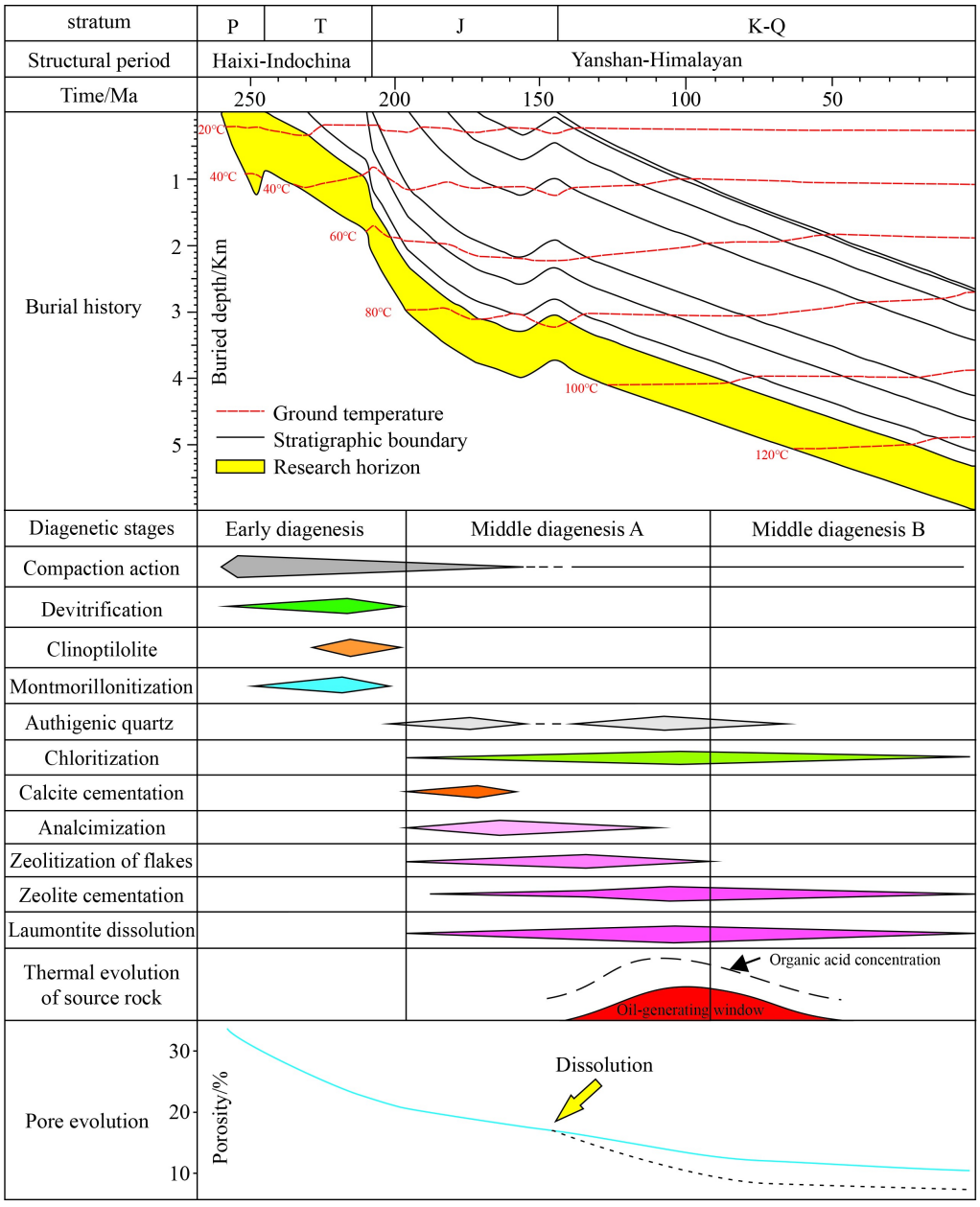

Fig. 11 Lower Wuerhe Formation reservoir burial evolution history and diagenetic evolution sequence diagram (Modified from Xi et al., 2015). P-Permian; T-Triassic; J-Jurassic; K-Cretaceous; Q-Quaternary.

References

Aase N E, Walderhaug O (2005). The effect of hydrocarbons on quartz cementation: diagenesis in the Upper Jurassic sandstones of the Miller field, North Sea, revisited. Petrol Geosci, 11(3): 215–223

Chen G Q, An Z Y, Abulimiti, Li X, Xu Q L, Zhang L F (2014). Petroleum exploration prospects of Carboniferous-Permian in peripheral Mahu Sag, Junggar Basin. Xinjiang Petrol Geo, 35(3): 259–263 (in Chinese)

Chen Z H, Zhai M, Zhu X M (2003). Relation between unconformity surface and hydrocarbon migration and accumulation of Luliang Uplift in Junggar Basin. J Palaeogeogr, 5(1): 120–126 (in Chinese)

Fu S, Pang L, Xu X L, Cao Y T, Liu Z Y, Zhang S C (2019). The characteristics and their controlling factors on reservoir in Permian Lower Urho Formation in Mahu Sag, Junggar Basin. Nat Gas Geosci, 30(4): 468–477 (in Chinese)

Gao C L, Ji Y L, Jin J, Wang J, Ren Y, Chen S Q, Wang R, Huan Z J (2017). Characteristics and controlling factors on physical properties of deep buried favorable reservoirs of the Qingshuihe Formation in Muosuowan Area, Junggar Basin. J Jilin U (Earth Sci Ed), 47(4): 990–1006 (in Chinese)

Gao P, Xiao X M, Hu D F, Liu R B, Li F, Zhou Q, Cai Y D, Yuan T, Meng G M (2022). Gas in place and its controlling factors of deep shale of the Wufeng-Longmaxi Formations in the Dingshan area, Sichuan Basin. Front Earth Sci, 17(1): 322–336

Guo M Z, Xu Y, Shou J F, Liu Z G, Han S H (2017). Controlling

factors of secondary pore development and petroleum exploration significance of Permian clastic rocks in northwest margin of Junggar Basin. Acta Sedimentola Sin, 35(2): 330–342 (in Chinese)

Han Y, Yang H B, Guo W J, Jiang W L, Wang T, Ren H J (2023). Hydrocarbon generation evolution and accumulation of Permian source rocks in the well PEN1 western depression of Junggar Basin. J Northeast Petrol U, 47(1): 30–43 (in Chinese)

He D F, Wu S T, Zhao L, Zheng M L, Li D, Lu Y (2018). Tectono‐depositional setting and its evolution during Permian to Triassic around Mahu Sag, Junggar Basin. Xinjiang Petrol Geo, 39(1): 35–47 (in Chinese)

He H Q, Zhi D M, Tang Y, Liu C W, Chen H, Guo X G, Wang Z S (2021b). A great discovery of Well Kangtan 1 in the Fukang Sag in the Junggar Basin and its significance. China Petrol Explor, 26(2): 1–11 (in Chinese)

He W J, Qian Y X, Zhao Y, Li N, Zhao X M, Liu G L, Miao G (2021a). Exploration implications of total petroleum system in Fengcheng Formation, Mahu Sag, Junggar Basin. Xinjiang Petrol Geo, 42(6): 641–655 (in Chinese)

Hou M C, Cao H Y, Li H Y, Chen A Q, Wei A J, Chen Y, Wang Y C, Zhou X W, Ye T (2019). Characteristics and controlling factors of deep buried-hill reservoirs in the BZ19-6 structural belt, Bohai Sea area. Nat Gas Indust, 39(1): 33–44 (in Chinese)

Hu X, Zou H L, Hu Z Z, Li Y P, Huang Y, Fu X P (2021). Reservoir characteristics and main controlling factors of glutenite reservoir in fan delta glutenite: a case study of the Upper Urho Formation of Permian in the east slope of Dongdaohaizi Sag, Junggar Basin. J Northeast Petrol U, 45(6): 15–26 (in Chinese)

Huang D J, Yu X H, Tan C P, Huang Fu Z Y, Zhai J H, Li H (2015). Pore structure features and its controlling factor analysis of reservoirs in Baikouquan formation, Maxi slope area. J Northeast Petrol U, 39(2): 9–18 (in Chinese)

Huang F X, Wang S Y, Li M P, Ouyang J L, Liu C, Liu H Y, Zeng F D, Fan J J, Jia P (2024). Progress and implications of deep and ultra-deep oil and gas exploration in PetroChina. Nat Gas Indust, 44(1): 86–96 (in Chinese)

Jia X L, He D F, Tong X G, Wang Z M (2011). Distribution of global giant oil and gas fields. China Petrol Explor, 16(3): 1–7 (in Chinese)

Jiang Y Q, Wen H G, Qi L Q, Zhang X X, Li Y (2012). Salt minerals and their genesis of the Permian Fengcheng Formation in Urho area, Junggar Basin. J Mineral Petrol, 32(2): 105–114 (in Chinese)

Lei H Y, Fan S, Xian B Z, Meng Y, Yang H X, Yan Q, Qi J (2020). Genesis and corrosion mechanism of zeolite of Lower Urhe Formation of Permian in Mahu Depression. Lithol Reserv, 32(5): 102–112 (in Chinese)

Li Y, Chen S J, Lu J G, Wang G, Zou X L, Xiao Z L, Su K M, He Q B, Luo X P (2020b). The logging recognition of solid bitumen and its effect on physical properties, AC, resistivity and NMR parameters. Mar Pet Geol, 112: 104070

Li Y, Xue Z J, Cheng Z, Jiang H J, Wang R Y (2020a). Progress and development directions of deep oil and gas exploration and development in China. China Petrol Explor, 25(1): 45–57 (in Chinese)

Li Z, Wu S H, Xia D L, He S, Zhang X (2018). An investigation into pore structure and petrophysical property in tight sandstones: a case of the Yanchang Formation in the southern Ordos Basin, China. Mar Pet Geol, 97: 390–406

Liu H J, Zhang C M, Gai S S, Yu W Z, Li J, Yuan H H, Zhang L, Liu H P (2024). Diagenetic facies identification and distribution prediction of Jurassic ultra-deep tight sandstone reservoirs in Yongjin Oilfield, Junggar Basin. Petrol Geo Recov Efficienc, 31(1): 13–22 (in Chinese)

Liu T X, Chen L, Bai S, Zhang J W, Qiao C, Cheng H, Tan X C, Qin H X (2025). Influence of sedimentary environment on the elastic characteristics of shale reservoirs: a case study of the Longmaxi Formation in the Zigong area, southern Sichuan. Acta Sedimentol Sin, 43(4): 1361–1370 (in Chinese)

Long L, Chen G Y, Yin S L, Fei X, Peng S J, Guo Q L (2021). Economic evaluation method of deep oil and gas fields based on different development stages. J Yangtze U (Nat Sci Ed), 18(5): 38–47 (in Chinese)

Ma Y P, Zhang X W, Huang L J, Wang G D, Zhang H, Pan S X (2021). Characteristics and controlling factors of glutenite reservoir rock quality of retrogradational fan delta: a case study of the Upper Wuerhe Formation of the Mahu Sag, the Junggar Basin. Energy Explor Exploit, 39(6): 2006–2026

Meng X C, Chen Y, Xie Y L, Guo H J, Luo X, Dou Y, Lu H G, Guo Z Y (2020). Prediction criteria of laumontite-bearing sand-conglomerate reservoirs and optimization of potential oil and gas accumulation areas: taking P_2w Formation in east slope of Mahu Sag as an example. J Northeast Petrol U, 44(3): 1–13 (in Chinese)

Pang D X (2015). Sedimentary genesis of sand-conglomerate reservoir and its control effect on reservoir properties: a case study of the lower Urho Formation in Ma 2 well block of Mahu Depression. Lithol Reserv, 27(5): 149–154 (in Chinese)

Pang X Q (2010). Key challenges and research methods of petroleum exploration in the deep of superimposed basins in western China. Oil Gas Geo, 31(5): 517–541 (in Chinese)

Qian H T, Su D X, Ablimiti Y, Wang X Y, Li Z H, Wang G D (2021a). Petroleum geological characteristics and exploration potential in slope area of Well Pen‐1 Western Depression in Junggar Basin. Nat Gas Geosci, 32(4): 551–561 (in Chinese)

Qian H T, Zhang X, Bian B L, Liu H L, Zhang M G (2021b). Characteristics and controlling factors of glutenite reservoir in Permian Lower Urho Formation in the south slope of the Mahu Sag. J Southwest Petrol U (Science & Technology Edition), 43(1): 41–50 (in Chinese)

Sun J, You X C, Zhang Q, Xue J J, Chang Q S (2023). Development characteristics and genesis of deep tight conglomerate reservoirs of Mahu area in Junggar Basin. Nat Gas Geosci, 34(2): 240–252 (in Chinese)

Tang Y, Wang Z Q, Pang Y Q, Deng S K, Wang C, Hong P H (2023). Hydrocarbon-generating potential of source rocks of Permian lower Urho Formation in western depression, Junggar Basin. Lithol Reserv, 5(15): 16–28 (in Chinese)

Tang Y, Xu Y, Li Y Z, Wang L B (2018). Sedimentation model and exploration significance of large-scaled shallow retrogradation fan delta in Mahu Sag. Xinjiang Petrol Geo, 39(1): 16–22 (in Chinese)

Tian J X, Ji B Q, Zeng X, Wang Y T, Li Y L, Sun G Q (2022).

Development characteristics and main control factors of deep clastic reservoirs of the Xiaganchaigou Formation in the northern marin of the Qaidam Basin, China. Journal of Nat Gas Geosci, 7(4): 225–235

Wang J D, Xu S M, Zhang G L, Zeng Z P, Ren X C, Wu X F, Shu P C, Feng H W (2022b). Reservoir physical properties and oil-bearing characteristics and main controlling factors of the Lower Jurassic Sangonghe Formation in the abdomen of Junggar Basin. Geol Rev, 68(3): 1129–1144 (in Chinese)

Wang J, Zhou J X, Liu M, Yang H X, Yang Z, Liao J D (2018). Sensitivity mechanism and evaluation of Permian lower Urho formation reservoir in Yanbei Area, Junggar Basin. Unconventional Oil Gas, 5(1): 28–34 (in Chinese)

Wang Q Y, Li S B, Yan W Q, Liu C W, Li H, Pan J, Liu X H (2023). Characteristics and main controlling factors of deep ultra-low porosity and ultra-low permeability glutenite reservoirs: a case study of the Upper Wuerhe Formation of Permian in Fukang Depression, Junggar Basin. J Northeast Petrol U, 47(2): 31–43 (in Chinese)

Wang Q, Liu W, Pei L, Cai Z, Luo H, Wang X, Zhang D, Liu J (2021). Hydrocarbon generation from calcium stearate: insights from closed-system pyrolysis. Mar Petrol Geo, 126: 104923

Wang R, Shi W Z, Xie X Y, Zhang W, Qin S, Liu K, Busbey A B (2020). Clay mineral content, type, and their effects on pore throat structure and reservoir properties: insight from the Permian tight sandstones in the Hangjinqi area, north Ordos Basin, China. Mar Petrol Geo, 115: 104281

Wang X J, Bai B J, Lu H, Liang Z L, Zhao C Y, Hu Y, Hu X, Li L (2022a). Characteristics and main controlling factors of deep ultra-deep glutenite reservoirs with high temperature and very strong overpressure: a case study from the Cretaceous Qingshuihe Formation in Gaoquan Area, Sikeshu Sag, southern margin of Junggar Basin. J Northeast Petrol U, 46(3): 54–65+8–9 (in Chinese)

Weibel R, Olivarius M, Jakobsen F C, Whitehouse M, Larsen M, Midtgaard H, Nielsen K (2019). Thermogenetic degradation of early zeolite cement: an important process for generating anomalously high porosity and permeability in deeply buried sandstone reservoirs. Mar Petrol Geo, 103: 620–645

Wu H G, Kang X, Qin M Y, Lian L X, Li J, Cao J (2022). Pore structure characteristics and genesis of heterogeneous conglomerate reservoir of Baikouquan Formation in Mahu sag, Junggar Basin. J Central South U (Sci Technol), 53(9): 3337–3353 (in Chinese)

Xi K L, Cao Y C, Wang Y Z, Girma H B, Zhang X X, Zhang J H, Jin J H (2015). Diagenesis and porosity-permeability evolution of low permeability reservoirs: a case study of Jurassic Sangonghe Formation in Block 1, central Junggar Basin, NW China. Petrol Explor Develop, 42(4): 434–443 (in Chinese)

Xia J J, He J Y, Ma L, Zhang J H (2012). Relationship between unconformity surface and reservoir forming of Permian, Madong 2 Slope. Nat Gas Explor Develop, 35(3): 9–12 (in Chinese)

Xu L, Chang Q S, Zhang N, Wang W, Zhu T (2018). Diagenesis and diagenetic facies of the reservoir in the Lower Wuerhe Formation of eastern Mahu Sag. Xinjiang Petrol Geo, 39(1): 76–82 (in Chinese)

Yao J, Huang C Q, Liu W Z, Zhang Y, Zeng D Q, Yan X (2018). Key mechanical problems in the development of deep oil and gas reservoirs. Scient Sin(Physica,Mechanica & Astronomica), 48(4): 044701(in Chinese)

Yin W, Zheng H R, Xu S L, Ma L J, Jia Q S, Wu X H (2008). An analysis on the process of hydrocarbon accumulation in the central depression belt of the Junggar Basin. Oil Gas Geo, 29(4): 444–452 (in Chinese)

Yu Q X, Zhou X W, Lu Q H, Duan T J, Li H (2023). Geochemical characteristics and oil-source correlation of the Upper Triassic source rocks in the northeastern margin of Junggar Basin. J Northeast Petrol U, 47(2): 44–54+7–8 (in Chinese)

Yuan G H, Cao Y C, Jia Z Z, Wang Y Z, Yang T (2015). Research progress on anomalously high porosity zones in deeply buried clastic reservoirs in petroliferous basin. Nat Gas Geosci, 26(1): 28–42 (in Chinese)

Yuan G H, Cao Y C, Qiu L W, Chen Z H (2017). Genetic mechanism of high-quality reservoirs in Permian tight fan delta conglomerates at the northwestern margin of the Junggar Basin, northwestern China. AAPG Bulletin, 101(12): 1995–2019

Zhang C Z (2021). Development mechanism and control factors of secondary pores in clastic rock. China Petrol Chem Stand Quality, 41(15): 138–139 (in Chinese)

Zhang L Y, Li J Y, Li Z, Zhang J G, Zhu R F, Bao Y S (2014). Advances in shale oil/gas research in North America and considerations on exploration for continental shale oil /gas in China. Adv Earth Sci, 29(6): 700–711(in Chinese)

Zhang Y P, Sheng S F, Gao X L (2015). Fan delta sedimentation and favorable reservoir distribution of the lower Urho Formation in Ma 2 well block of Mahu Depression. Lithol Reserv, 27(5): 204–210 (in Chinese)

Zhang Z P, Zhang Y, Zhang M L, Lu H M, Zhang R Q, Chen Y Z, Wang H Z, Li P W (2022). Main controlling factors and exploration direction of Permian to Triassic reservoir in the central sag of Junggar Basin. Petrol Geo Exper, 44(4): 559–568 (in Chinese)

Zhou J J, Wu H G, Wang J, Hu G, Zhang Y F, Feng J L, Li Y L (2023). Quantitative assessment of the effects of zeolite alteration processes on deep clastic reservoirs – A case study of the Jiamuhe Formation in the Shawan Sag, Junggar Basin, China. Mar Petrol Geo, 154: 106286

Zou N N, Zhang D Q, Shi J A, Lu X C, Zhang S C (2021). Formation conditions and main controlling factors of hydrocarbon accumulation of the upper Wuerhe Formation of Permian in Zhongguai Uplift, Junggar Basin. Nat Gas Geosci, 32(4): 540–550 (in Chinese)